JOURNAL OF SPACECRAFT AND ROCKETS
Vol. 36, No. 6, November–December 1999

Presented here are five papers on large-scale analyses of a complex shell structure. The first, longer paper, "Nonlinear Behavior of Space Shuttle Superlightweight Liquid-Oxygen Tank Under Prelaunch Loads," covers the structure, the analysis technique, some loading cases, and experimental verification on the method. It is followed by a companion paper, "Modeling and Nonlinear Structural Analysis of a Large-Scale Launch Vehicle," which goes into greater depth on the methods, and then by three shorter papers, "Effects of Welding-Induced Imperfections on Behavior of Space Shuttle Superlightweight Tank," "Nonlinear Behavior of Space Shuttle Superlightweight Tank Under Booster Ascent Loads," and "Nonlinear Behavior of Space Shuttle Superlightweight Tank Under End-of-Flight Loads," covering interesting behavior under differing load cases. These papers are intended to stand on their own (and hence have some redundant introductory material) but are complementary to one another, and so they are presented here together.

Nonlinear Behavior of Space Shuttle Superlightweight Liquid-Oxygen Tank Under Prelaunch Loads

Michael P. Nemeth,* Vicki O. Britt,† Richard D. Young,‡ Timothy J. Collins,§ and James H. Starnes Jr.¶
NASA Langley Research Center, Hampton, Virginia 23681-2199

The new Space Shuttle superlightweight external fuel tank flew for the first time on 2 June 1998 (Space Transportation System-mission 91). We present results of elastic linear-bifurcation buckling and nonlinear analyses of one of its major components; that is, the liquid-oxygen tank. The contents include an overview of the structure and a brief description of the finite element code that was used to conduct the analyses. Results are presented that illustrate three distinctly different types of nonlinear response phenomena for thin-walled shells that are subjected to combined mechanical and thermal loads that launch-vehicle shell designers may encounter. A procedure is demonstrated that can be used by structural analysts and designers to obtain reasonable, conservative estimates of linear-bifurcation, buckling-load knockdown factors for shells that are subjected to complex loading conditions or to characterize the effects of initial geometric imperfections on nonlinear shell response phenomena. Results are also presented that show that the superlightweight liquid-oxygen tank can carry loads in excess of twice the values of the operational prelaunch loads considered and that a fluid-filled launch-vehicle shell can be highly sensitive to initial geometric imperfections.

Introduction

THE new era of international cooperation in space has created the need for the Space Shuttle to reach a 51.6-deg, high-inclination orbit. Until recently, achieving this orbit required the payload of the orbiter to be reduced by approximately 10,000 lb. To recover most of the lost payload and to faciliate construction of the International Space Station, NASA began development of a new, lighter-weight external fuel tank for the Space Shuttle that is made primarily from an aluminum–lithium alloy and that has substantially thinner shell walls. This new design, referred to by NASA as the superlightweight (SLWT) tank, weighs approximately 58,000 lb, which is approximately 8000 lb lighter than the lightweight aluminum external tank previously in service. The new SLWT external tank flew for the first time on 2 June 1998 on the last Space Shuttle mission to the MIR Space Station (Space Transportation System-mission 91).

An important consideration in the design of the SLWT tank was the nonlinear behavior of the thin-walled regions of the structure that experience compressive stresses. Local buckling, global buckling, or excessive stable, wrinklelike bending deformations of the shell wall can cause the thermal protection system (TPS) to separate from the tank, which could cause the vehicle to fail. Typically, in designing a thin-walled shell structure like the SLWT tank, the effects of small initial geometric imperfections on the stability of the structure must be considered to obtain a meaningful estimate of the buckling-load level for a given loading condition. However, the effects of small initial geometric imperfections on the stability of even simple shell geometries that are subjected to combined mechanical and thermal loadings are not generally known and are often estimated in an ultaconservative and contrived manner from known results for simple shell geometries that are subjected to simple loading conditions. In addition, complex shell structures like the SLWT tank may exhibit nonlinear response phenomena that may not be represented adequately by a contrived shell behavioral model. Certainly, the effects of small initial geometric imperfections can be obtained for specific structural configurations by using carefully designed, probably large-scale, experiments. However, this approach can be costly and can have significant, undesirable effects on a production schedule. Thus, it is beneficial to have an analysis approach for problems of this nature that captures adequately the possible nonlinear response phenomena and the effects of small initial geometric imperfections. With these considerations in mind, and to ensure that the SLWT tank design does not have a shell-wall instability response or undesirable wrinklelike bending deformations, meaningful finite element analysis predictions of the nonlinear response of the SLWT tank were sought by NASA.

One component of the SLWT tank that experiences significant compressive stresses is the liquid-oxygen (LO_2) tank. A primary goal of the SLWT tank study that has been conducted by NASA was to determine how much additional load, beyond the operational loads for two critical prelaunch loading conditions and two critical flight loading conditions, the LO_2 tank can withstand before buckling or exhibiting wrinklelike bending deformations that can lead to failure of the TPS. Toward that goal, this paper presents results of large-scale elastic linear-bifurcation buckling and nonlinear finite element analyses of the SLWT LO_2 tank that were conducted by NASA Langley Research Center personnel for the two prelaunch loading conditions. In addition, results are presented for two full-scale structural tests of the original standard-weight (SWT) LO_2 tank configuration that differs primarily in shell wall thickness, weight, and material type from the SLWT LO_2 tank. These two tests were conducted nearly 20 years ago and are the only tests available that exhibit a buckling event in the LO_2 tank. Because the SWT LO_2 tank is so geometrically similar to the SLWT LO_2 tank, results for these tests were obtained to gain confidence in the finite element modeling approach used in the present study and to demonstrate

Received 24 September 1997; revision received 17 April 1999; accepted for publication 2 July 1999.

*Senior Research Engineer, Structural Mechanics Branch, Structures Division. Associate Fellow AIAA.
†Aerospace Engineer, Structural Mechanics Branch, Structures Division; currently with Gulfstream Aerospace Corp. Member AIAA.
‡Aerospace Engineer, Structural Mechanics Branch, Structures Division. Member AIAA.
§Aerospace Engineer, Structural Mechanics Branch, Structures Division.
¶Head, Structural Mechanics Branch, Structures Division. Fellow AIAA.

that the approach yields meaningful representations of the nonlinear structural response of the SLWT LO_2 tank.

A primary objective of the present paper is to illustrate a large-scale finite element analysis approach that is used in the present study to show that the SLWT LO_2 tank can sustain load levels in excess of the operational load levels of the two prelaunch loading conditions, and to provide results that can be used to gain insight into the performance of the TPS. These results demonstrate a simple way of obtaining information from the finite element results that can be useful for assessing the performance of TPS for future launch vehicles. This illustration demonstrates a practical means for assessing or verifying the nonlinear response of complex launch-vehicle structures, and sensitivity of the response to small initial geometric imperfections, that could be used in some cases possibly as a viable alternative to, or at least a complement to, large-scale structural testing. Another objective is to illustrate some of the generic aspects of the SLWT tank analyses that could be applicable to the analysis and design of other liquid-fuel launch vehicles. First, an overview of the SLWT LO_2 tank and intertank structure and the loading conditions are presented. Then, the analysis code is briefly discussed, and the results of the elastic, linear-bifurcation buckling analyses and the nonlinear analyses are presented. The number of details used to construct the finite element models that were used in the present study are enormous, and as a result, many of the details are not presented herein. To highlight some of the generic shell-analysis aspects, a detailed discussion of the nonlinear response phenomena that were exhibited by the SWT LO_2 tank and encountered in the present study is given. This discussion includes the sensitivities of the response phenomena to initial geometric imperfections. Moreover, the significance of using linear-bifurcation buckling analyses to characterize or represent the nonlinear behavior and the use of buckling-load knockdown factors to represent the effects of initial geometric imperfections are discussed. These two analysis elements encompass the traditional approach that is commonly used by industry for the preliminary design of shell structures.

In analyzing the SLWT LO_2 tank and the two structural tests, and in presenting the results, a specific procedure is used in the present study to articulate the nonlinear behavior associated with each loading condition. First, results of elastic, linear-bifurcation buckling analyses are presented. Then, results of nonlinear analyses of the geometrically perfect, elastic shell and the elastic shell with an initial geometric imperfection in the form of the linear-bifurcation buckling mode are presented. This procedure is not new (e.g., see Ref. 1), and although it is presented in the present paper for a specific launch vehicle, it is a procedure that can be applied to large problems like the design of future liquid-fuel launch vehicles or to smaller problems like the analysis of simple shell components that are subjected to simple loadings. In addition to characterization of the nonlinear behavior, the procedure can be used to obtain reasonable, not too overly conservative, estimates of linear-bifurcation, buckling-load knockdown factors for doubly curved shells that are subjected to complex loading conditions. These buckling-load knockdown factors are intended to reflect reductions in load-carrying capacity of a shell that are caused by initial geometric imperfections. Generally, buckling-load knockdown factors, or imperfection sensitivity estimates, for shells with compound curvature that are subjected to simple or complex loading conditions are unknown. For shell structures like the SLWT LO_2 tank, estimates of imperfection sensitivity for combined loadings are often obtained by crude engineering approaches and are typically ultraconservative, which usually results in higher cost. Thus, the analysis procedure used in the present paper demonstrates in detail a means for eliminating unnecessary conservatism from preliminary designs that involve shell stability.

Overview of the SLWT Tank Structure

The Space Shuttle consists of the orbiter, two solid rocket boosters (SRBs), and the external tank (ET), as shown in Fig. 1. The ET consists of a LO_2 tank, a liquid-hydrogen (LH_2) tank, and an intermediate structure called the intertank (Fig. 1). The intertank transmits the weight of the fuel, the ET structural weight, and the orbiter weight to the SRBs prior to launch and transmits thrust loads from the SRBs and the orbiter to the ET during ascent. The LO_2 tank is

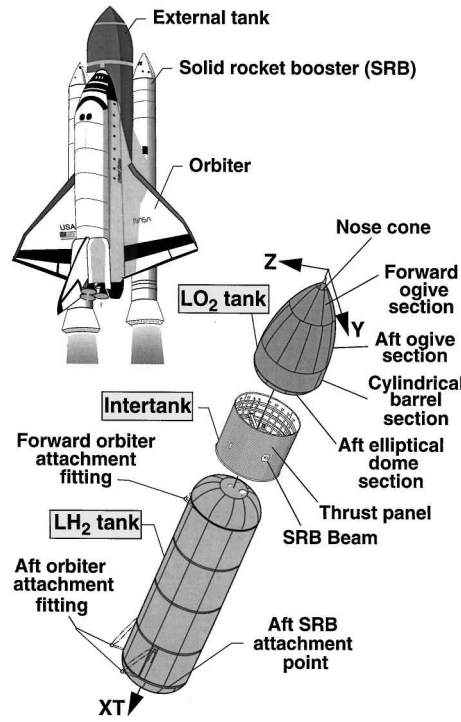

Fig. 1 Space Shuttle ET components.

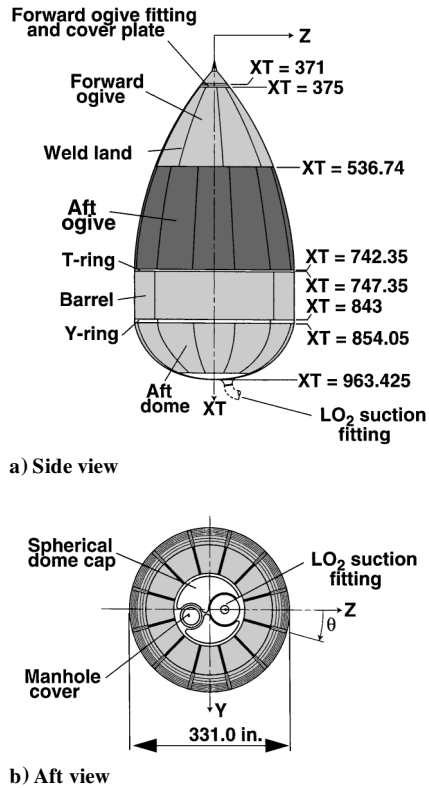

Fig. 2 LO_2 tank components; values of XT are given in inches.

a thin-walled monocoque shell made primarily of 2195 aluminum–lithium alloy, and is approximately 49 ft long and has a maximum diameter of approximately 27.5 ft, as indicated in Fig. 2. The LO_2 tank consists of a forward-ogive section made from 8 gore panels, an aft-ogive section made from 12 gore panels, a cylindrical barrel section made from 4 barrel panels, and an aft elliptical dome section made from 12 gore panels. The coordinate systems used to locate the elements of the LO_2 tank and the intertank are also shown in Fig. 2. The coordinates (XT, Y, Z) are typically referred to as the global coordinate system of the ET, and axial positions along the tank are

indicated by the coordinate value of XT in inches. For example, the junction between the forward and aft ogives is indicated by writing $XT = 536.74$ in. Cylindrical coordinates are also used and are given by (r, θ, XT), where a positive value of θ is measured from the positive Z axis toward the positive Y axis, as shown in Fig. 2.

The LO_2 tank also has a forward T-ring and an aft Y-ring frame that supports a baffle that prevents the fuel from sloshing during ascent. The slosh baffle, a lightweight (approximately 455 lb), thin-walled structure, is supported by two deep, thin-walled rings at each end that attach to the forward T-ring and the aft Y-ring frame. Other parts of the LO_2 tank include a nonstructural nose cone, a forged forward-ogive fitting and cover plate, an aft spherical dome cap that contains the LO_2 suction fitting and a covered manhole, and a vortex baffle attached to the base of the aft dome cap. The LO_2 tank gore and barrel panels are stretch formed, chemically milled, and then welded together. The panels are fabricated with substantial thickness tailoring to reduce structural weight. The thickness distributions of the panels are very complex and as a result are not presented herein. A qualitative example of the extent of the thickness tailoring in the aft ogive is given in Ref. 2. The panels are made somewhat thicker at the welds to form a stiffenerlike region that is used as a weld land. The primary role of the weld lands is to compensate for any reduction in shell-wall strength that is caused by welding. Tapering the weld lands in thickness and width along their length reduces weight and alleviates stress concentrations in the shell that result from abrupt changes in thickness.

The intertank is a right-circular cylinder that is made from 2090 aluminum–lithium and 7075 aluminum alloys and is shown in Fig. 3. The approximately 22.5-ft-long intertank has a diameter of approximately 27.5 ft and consists of six 45-deg curved panels that are stiffened longitudinally with external hat stiffeners and are referred to herein as skin-stringer panels. The intertank also has two massive 45-deg curved panels, referred to as thrust panels, located perpendicular to the Y axis of the intertank (Fig. 3) that are stiffened longitudinally with integrally machined external blade stiffeners. These eight panels are assembled into the intertank with mechanical fasteners and are attached to five large internal ring frames, a forward flange, and an aft flange. Longitudinal straps (referred to herein as roll ties) suppress lateral-torsional deflection of the ring frames. The main central ring frame, two thrust panel longerons, and the thrust panels are connected to each end of a tapered beam that is referred to herein as the SRB beam (Fig. 3). The SRB beam spans the diameter of the intertank along the Y axis and has a maximum depth (in the XT direction) of approximately 43 in. at its midspan. Forged fittings (referred to herein as SRB thrust fittings) that are incapable of transmitting moments are fastened to the ends of the SRB beam. The primary role of the thrust panels is to diffuse the large axial loads introduced by the SRBs into the intertank and then into the LO_2 tank shell wall. The SRB beam compensates for the eccentricity of the concentrated loads introduced by the SRBs. The SRB beam also supports the loads normal to the intertank (parallel to the SRB beam) at the SRB attachment points. The intertank also has a 46 in. high × 52 in. wide frame-reinforced nonstructural access door located along the cylinder generator at approximately $\theta = 146$ deg.

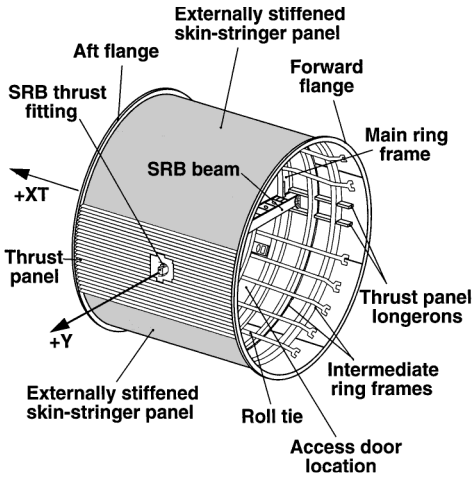

Fig. 3 Intertank components.

Critical Prelaunch Loading Conditions

Two critical SLWT tank prelaunch loading conditions and two critical in-flight loading conditions were identified and supplied by the members of the SLWT tank structural verification team at the NASA Marshall Space Flight Center and at the Lockheed Martin Manned Space Systems Division. The general characteristics of the critical loads are indicated in Fig. 4. These loads consist of the wind or aerodynamic pressure loads, the structural weight or inertia, the pressure exerted on the shell wall by the LO_2, the ullage pressure inside the tank, the interface forces exerted by each SRB shown in Fig. 1 (indicated by the vectors $\boldsymbol{R}_1$ and $\boldsymbol{R}_2$ in Fig. 4), the interface forces between the intertank and the LH_2 tank (indicated by the vectors $\boldsymbol{F}$ and $\boldsymbol{M}$ in Fig. 4), and the thermally induced loads associated with the cryogenic-fuel temperatures. These loading conditions correspond to worst-case conditions, and as a result, no attempts are made in the present study to address issues of loading imperfections or perturbations, with the exception of the wind loading.

The two critical loading conditions that are addressed herein correspond to prelaunch fueling conditions that occur when the Space Shuttle is on the launch pad. Prior to launch, the LH_2 tank is filled with LH_2, and then the LO_2 tank is filled with LO_2. The first loading condition considered corresponds to a full LH_2 tank and an empty LO_2 tank. For this condition, there is no pressure and no temperature change in the LO_2 tank. However, the lower 45 in. of the intertank are subjected to an axisymmetric, uniform through-the- thickness temperature field that varies linearly from −423°F, where the intertank is attached to the LH_2 tank, to 50°F at the top of the LH_2 tank forward dome. The nominal ambient temperature of the LO_2 tank and the intertank prior to fueling is 50°F. The SRB interface forces (kips; 1 kip = 1000 lb) that were supplied by the SLWT tank structural verification team are given by

$$\boldsymbol{R}_1 = -224.092\boldsymbol{i} - 52.223\boldsymbol{j} - 28.954\boldsymbol{k} \tag{1}$$

$$\boldsymbol{R}_2 = -343.624\boldsymbol{i} + 48.261\boldsymbol{j} - 30.754\boldsymbol{k} \tag{2}$$

where the vectors $\boldsymbol{R}_1$ and $\boldsymbol{R}_2$ are shown in Fig. 4 and where $\boldsymbol{i}$, $\boldsymbol{j}$, and $\boldsymbol{k}$ are standard orthonormal base vectors associated with the XT, Y, and Z axes, respectively. Similarly, the interface force (kips) and moment (in.-kips) between the intertank and the LH_2 tank are given by

$$\boldsymbol{F} = 541.593\boldsymbol{i} + 9.614\boldsymbol{j} + 63.494\boldsymbol{k} \tag{3}$$

$$\boldsymbol{M} = -310.500\boldsymbol{i} + 10{,}715.745\boldsymbol{j} + 16{,}828.589\boldsymbol{k} \tag{4}$$

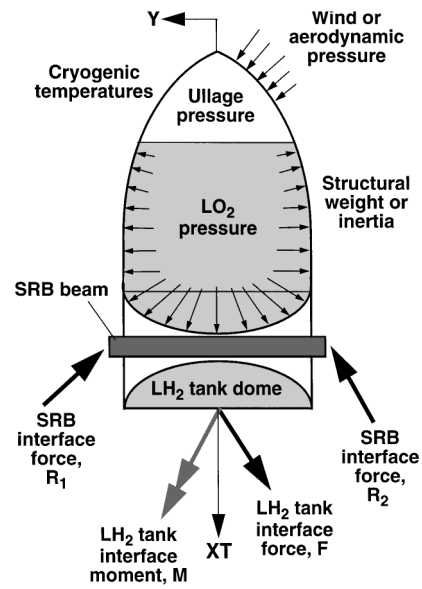

Fig. 4 Loading characteristics.

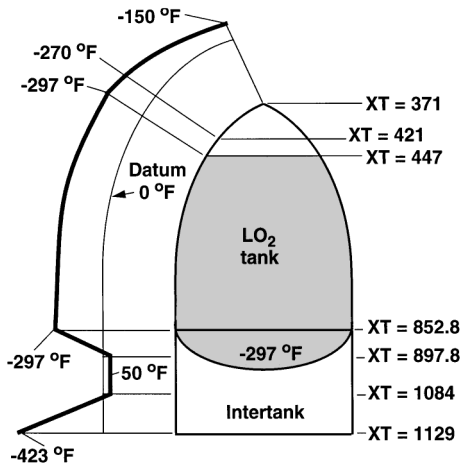

Fig. 5 Axisymmetric temperature profile for prelaunch loading condition with full LH_2 and LO_2 tanks; values of XT are given in inches; nominal ambient temperature = 50°F.

The LO_2 tank is also subjected to wind pressure that has a resultant force given by $-5.652\boldsymbol{j} - 3.786\boldsymbol{k}$ kips. Comparison of the magnitude of the wind load with the other loads that act on the structure indicates that the wind load is relatively small. The actual wind pressure distribution that was input into the finite element models is somewhat complicated and, as a result, is not presented herein.

The second prelaunch loading condition considered corresponds to full LH_2 and LO_2 tanks, but without ullage pressure. For this condition, the LO_2 tank is filled to $XT = 447$ in. (see Fig. 2), which corresponds to a depth of approximately 43 ft. For this case, the hydrostatic pressure distribution in the LO_2 tank is essentially axisymmetric. Asymmetry in the pressure distribution is caused by the eccentric weight of the orbiter, is relatively small, and is neglected. The specific weight of the LO_2 used in the present study is 0.04123 lb/in.[3], and the maximum hydrostatic gauge pressure is approximately 21 psi at the bottom of the tank. The corresponding weight of the LO_2 is approximately 1348 kips.

For the second prelaunch loading condition, the temperature distribution in the LO_2 tank and the intertank is axisymmetric and uniform through-the-thickness, and is shown in Fig. 5. The temperature field for the LO_2 tank has a uniform value of -297°F between $XT = 447$ and 852.8 in., but varies from a value of -150°F at the nose to -297°F at the free surface of the LO_2 ($XT = 447$ in.). The intertank is subjected to a temperature field that varies in a piecewise linear manner from -423 to 50°F and then to -297°F as the intertank is traversed from $XT = 1129$ to 852.8 in. The temperature field shown in Fig. 5 represents the changes in the temperature distribution that occur from the nominal, uniform prefueling temperature of 50°F, and the corresponding thermally induced loads.

The SRB interface forces (kips) that were supplied by the SLWT tank structural verification team for the second prelaunch loading condition are given by

$$\boldsymbol{R}_1 = -906.447\boldsymbol{i} - 105.605\boldsymbol{j} - 30.502\boldsymbol{k} \tag{5}$$

$$\boldsymbol{R}_2 = -1035.789\boldsymbol{i} + 108.128\boldsymbol{j} - 32.557\boldsymbol{k} \tag{6}$$

Likewise, the interface force (kips) and moment (in.-kips) between the intertank and the LH_2 tank are given by

$$\boldsymbol{F} = 568.113\boldsymbol{i} + 3.014\boldsymbol{j} + 66.913\boldsymbol{k} \tag{7}$$

$$\boldsymbol{M} = -354.488\boldsymbol{i} + 11{,}249.318\boldsymbol{j} + 19{,}443.206\boldsymbol{k} \tag{8}$$

and the LO_2 tank is subjected to a wind load with a resultant force given by $-5.537\boldsymbol{j}$–$3.854\boldsymbol{k}$ kips. Once again, comparison of the magnitude of the wind load with the other loads acting on the structure indicates that the wind load is also relatively small for this loading condition. The actual wind pressure distribution that was input into the analysis models is not presented herein because of its somewhat complicated nature.

Analysis Code and Finite Element Modeling

The results of the elastic, linear-bifurcation buckling and nonlinear analyses were obtained with the STAGS nonlinear structural analysis code for general shells.[3] The finite element models of the SLWT tank used in the present study are very complex and include many structural details and the skin thickness variations or tailoring used to reduce structural weight; for example, see Ref. 2. STAGS was chosen for analyzing the SLWT tank because of its robust state-of-the-art nonlinear-equation solution algorithms and its general user-input capability that is convenient for modeling branched shells that are typically used for launch vehicles. The shell elements that were used to model the SLWT tank response are based on classical thin-shell theory. The use of these elements is justifed from a practical perspective because the ratio of the wall thickness to the minimum radius of curvature at each point of the undeformed LO_2 tank is typically much less than 0.1, and, as will be shown, because the ratio of the largest thickness of the shell wall that forms a given deformation pattern to the smallest characteristic length of the deformation pattern is less than 0.1 (Refs. 4–6). A description of the attributes of STAGS and how the features of STAGS were used in the present study to model the SLWT LO_2 tank and intertank are presented in Refs. 2 and 7. The finite element modeling details for the SLWT LO_2 tank and intertank are lengthy and are not presented herein; they are discussed in Refs. 2 and 7. Details of how the applied loads were simulated, how mesh refinements were conducted, and how sensitivity to initial geometric imperfections was assessed are presented subsequently.

Load Simulation

A primary goal of the SLWT LO_2 tank study was to determine a meaningful estimate of how much additional load, beyond the operational loads, the tank can withstand before buckling or exhibiting excessive bending deformations that will damage the thermal protection system. The basic approach used in the present study to achieve this goal is to apply all of the loads illustrated in Fig. 4 to the given finite element model, except for the SRB interface loads. In the finite element model, the nodes on the ends of the SRB beam, where the SRB forces act, were restrained so that the SRB interface forces became reactions and rigid-body motion was eliminated. The simple LO_2 pressure distribution and the temperature distribution were input into the STAGS models with the user-written Fortran subroutines to provide a spatial description which faciliates finite element mesh refinement. The substantially more complicated wind load, given as a discrete force field, was approximated by a Fourier series representation that was also input directly into the STAGS models with a user-written Fortran subroutine, to faciliate finite element mesh refinement. The slosh baffle weight of approximately 455 lb was applied to the slosh baffle support rings at $XT = 744.85$ and 851.0 in. (see Fig. 2) as eccentric, uniformly distributed line loads. The LH_2 tank interface force and moment were applied to the model with the least-squares loading and moving plane boundary features of STAGS.[2] The STAGS least-squares loading feature used a least-squares fit to convert concentrated forces and moments applied at an axial location into statically equivalent shell-wall stress resultants. The moving plane boundary feature of STAGS enforced the geometric constraint that all nodes within the given plane remain coplanar during deformation, which is consistent with the high stiffness of the intertank at the LH_2 tank interface.

Next, the applied loads were separated into two groups. The first group contains the LH_2 tank interface force and moment, which were indentified by the SLWT tank structural verification team as the primary source of destabilizing compressive stresses in the LO_2 tank that may occur at load levels greater than the corresponding operational load level. The second group of loads consisted of the LO_2 pressure (for the second loading condition), the wind load, the structural weight, the thermal load, and the weight of the slosh baffle located inside the barrel section of the LO_2 tank. Constant in value, the loads in the second group were identified by the SLWT tank structural verification team as part of the operational loads that are considered to be passive loads when determining the stability margin of safety of the LO_2 tank.

In performing linear-bifurcation buckling and nonlinear analyses with STAGS, two load factors, p_a and p_b, were assigned to the first (active) and second (passive) load groups, respectively. First, a linear analysis was conducted to verify that the SRB reactions calculated from the applied loads were reasonably close to the specified values given herein. Differences between the SRB reactions computed for a specific finite element model and the corresponding forces that were given arise, to some exent, from discrepancies in the structural geometry that yield small errors in the calculated structural mass and the resultant force of the applied LO_2 pressure. These discrepancies arise, for the most part, from the discretization of the curved, variable thickness surfaces with flat finite elements and the use of a simplified finite element representation of the intertank. Another source of discrepancies arises from the approximation of the wind pressure by the Fourier series representation.

For both prelaunch loading conditions, the $\boldsymbol{i}$ components of the reactions, which are the largest source of destabilizing stresses in the LO_2 tank, and the $\boldsymbol{k}$ components were in excellent agreement with the corresponding specified values, with differences less than approximately 1.5%. In contrast, the $\boldsymbol{j}$ components of the reactions were not in very good agreement with the specified values. These discrepancies were caused inadvertently and, for the most part, by restraining the elongation of the SRB beam. However, because the $\boldsymbol{j}$ components of the reactions act along the axis of the SRB beam, their effect is mostly contained within the central region of the intertank. As a result, the SRB beam reactions are reasonable approximations to the actual forces and were judged by the SLWT tank structural verification team to provide an adequate representation of the actual load transfer from the intertank to the LO_2 tank.

For the linear-bifurcation buckling analyses, the load factor for the passive load group was assigned a value of one ($p_b = 1$) and the load factor for the active load group p_a was defined as the eigenvalue. Setting $p_b = 1$ defines a fixed-magnitude linear prebuckling state that is not scaled by the eigenvalue. In particular, STAGS uses both the prebuckling membrane stress state and prebuckling deformations of the passive loads to compute the overall stiffness matrix of a structure. Moreover, STAGS uses only the prebuckling stress state of the active loads to compute the overall geometric stiffness matrix. A discussion of this approach is found in Ref. 8. Thus, the linear-bifurcation analysis of STAGS for structures with a fixed, passive set of loads is not the same as bifurcation analyses found in the literature that use only the linear, membrane prebuckling stress state.

For the nonlinear analyses, the load factors for both load groups were increased simultaneously to a value of one ($p_a = p_b = 1$), which corresponds to the operational values of the loads and provides the proper nonlinear prebuckling state for the LO_2 tank. Then the load factor p_a of the primary destabilizing loads was increased until an instability was reached or the operational loads were substantially exceeded.

Mesh Refinement Procedure

In the process of conducting the analyses for the present study, several different finite element models with different levels of mesh refinement were developed for each loading condition considered. The goal of the mesh refinement procedure was to identify finite element models that predict adequately the nonlinear structural response, yet had as few degrees of freedom (DOF) as reasonably possible. To identify the mesh required for a given loading condition, it is necessary to determine the regions of the structure that buckle and to determine the characteristic wavelengths of the buckle patterns. Because the location of the buckled regions and the buckle patterns depend on the loading condition, the following mesh refinement procedure was repeated for each loading condition.

A series of linear-bifurcation buckling analyses were conducted to obtain a finite element mesh that yields a converged minimum eigenvalue. Starting with a uniform mesh, modifications were made to models iteratively in which the buckled regions were made more refined and unneeded mesh refinement was eliminated elsewhere, with care taken not to introduce spurious solutions. Variations in the mesh refinement were facilitated by the use of the five-node and seven-node rectangular transition elements available in STAGS.[2,3] Convergence was evident when doubling the refinement in the buckled regions of the LO_2 tank had little effect on the minimum eigenvalue. Nonlinear analyses were then conducted with the finite element model with the greatest refinement in the buckled regions and also with the corresponding model that had one less level of refinement. This step was done to confirm that there was little difference between the nonlinear solutions for the models with the two levels of mesh refinement. In the mesh refinement studies, a rule of thumb was used that dictated that the finite element mesh should have a minimum of four elements per half-wave in the bending deformations.

Geometric Imperfection Sensitivity

An important consideration in the present study is the effects of initial geometric imperfections. Linear-bifurcation buckling-mode imperfection shapes were used in the analysis because measured inital geometric imperfection data were not available and because this type of imperfection is thought to yield, if not the worst, a high degree of imperfection sensitivity.[9] This statement is rationalized by noting that the linear-bifurcation buckling mode represents an adjacent equilibrium state that the structure has an intrinsic affinity to deform into, provided that there are no substantial nonlinear prebuckling effects present. Moreover, in the absence of substantial nonlinear prebuckling effects, the linear-bifurcation buckling mode is similar to one or more of the dominant, unstable nonlinear deformation states that the geometrically perfect structure passes through at buckling, and an imperfection in the form of the linear-bifurcation buckling mode provides a mechanism for a relatively early departure, with a preferred direction, from the primary equilibrium path of the structure. When substantial prebuckling deformations are present, the linear prebuckling stress state does not provide an accurate estimate of the stress state for higher values of the load factor. Thus, bifurcation buckling modes obtained with a linear prebuckling stress state may not be similar to the dominant, unstable nonlinear deformation states and may not provide a mechanism for a relatively early departure from the primary equilibrium path of the structure.

In general, the sign of the linear-bifurcation buckling mode is arbitrary and is determined by the specific algorithm used to perform the calculations. For a shell structure with nonnegative Gaussian curvature, the sign of the buckling mode (eigenvector) indicates whether a specific region of the buckling mode of a curved surface is directed toward or away from the concave side of the surface. As a result, these two orientations of the same buckling mode generally correspond to different degrees of nonlinear interaction between the imperfection shape and the membrane compressive stresses. In the present study, the negative of the linear-bifurcation buckling modes obtained from the STAGS models were used as the imperfection shapes because it was found, for every case presented herein, that they provide the strongest nonlinear interaction with the compressive stresses in the shell wall.

Results for SLWT Tank Prelaunch Loads

Results are presented in this section for the two prelaunch loading conditions discussed earlier. First, results are presented for the loading condition that has a full LH_2 tank and an empty LO_2 tank. Then, results are presented for the loading condition that has a full LH_2 tank and a full LO_2 tank. For this second loading condition, results are presented that were obtained from STAGS models that neglect the slosh baffle ring stiffnesses. To determine the effect of neglecting the slosh baffle ring stiffnesses, additional results were obtained with models that include these ring stiffnesses. Comparison of these results shows that neglecting the slosh baffle ring stiffnesses in the STAGS models yields similar structural deformations and the lower, more conservative prediction of the LO_2 tank load-carrying capacity at load levels greater than the level of the operational loads. For both prelaunch loading conditions, results were also obtained with and without the relatively small wind loads. Neglecting the wind loads was found to have an essentially negligible effect on the results. The results that are presented are for no wind loads.

Full LH_2 and Empty LO_2 Tanks

The models that were investigated for this prelaunch loading condition range from 104,600 to 213,500 DOF. The model that was

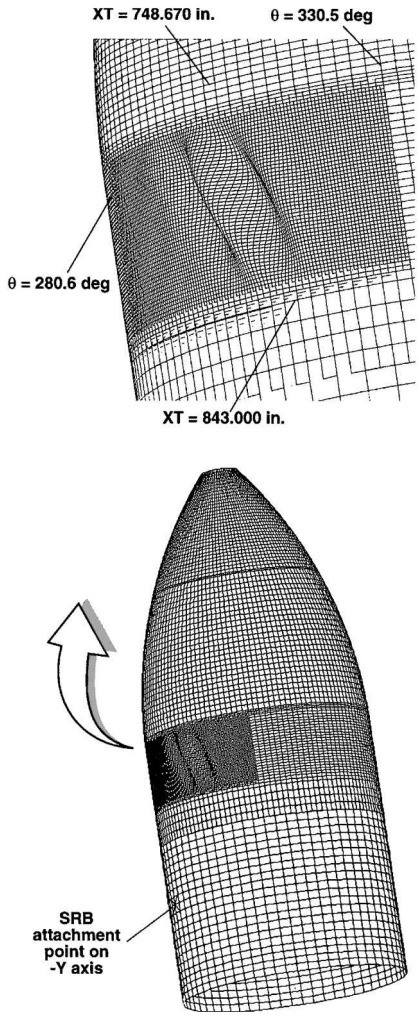

Fig. 6 Linear-bifurcation buckling mode for prelaunch loading condition with full LH_2 tank and empty LO_2 tank; 146,700 DOF, p_a = 3.26, and p_b = 1.0.

identified as adequate for predicting the linear-bifurcation buckling behavior is shown in Fig. 6 and corresponds to 146,700 DOF. Figure 6 shows a buckle in the LO_2 barrel on the negative Y-axis side of the tank. The 104,600- and 146,700-DOF models have the same general mesh arrangement shown in Fig. 6, but the level of local refinement of the mesh shown in Fig. 6 for the 146,700-DOF model is essentially twice that of the 104,600-DOF model. The eigenvalues for the 104,600- and 146,700-DOF models are given by $p_a = 3.36$ and 3.26, respectively. These values correspond to active (destabilizing) loads that are approximately three times the magnitude of the corresponding operational loads. Based on the smoothness of the buckling mode shown in Fig. 6 and the 3% difference in the eigenvalues, the 146,700-DOF model is considered adequate for representing the linear-bifurcation buckling behavior of the LO_2 tank for this loading condition. In addition, the ratio of the largest thickness in the area of the buckling mode shown in Fig. 6 to its smallest characteristic length is less than 0.1, which indicates that finite elements that are based on classical thin-shell theory are adequate.

Next, the 104,600- and 146,700-DOF models were used to conduct nonlinear analyses of a geometrically imperfect shell. An imperfection shape in the form of the corresponding linear-bifurcation buckling mode with a negative amplitude and with an imperfection-amplitude-to-wall-thickness ratio $A/t = 0.25$ was used in these analyses. The thickness t in the ratio A/t, the minimum wall thickness for the LO_2 barrel, has a value equal to 0.140 in. The results of these analyses, shown in Fig. 7, are presented as a plot of load factor p_a vs the normal displacement of the shell wall at the largest crest of the buckle defined by the coordinates $XT = 787.97$ in. and $\theta = 300.94$ deg. (See Fig. 2 for coordinate definitions.) The dashed

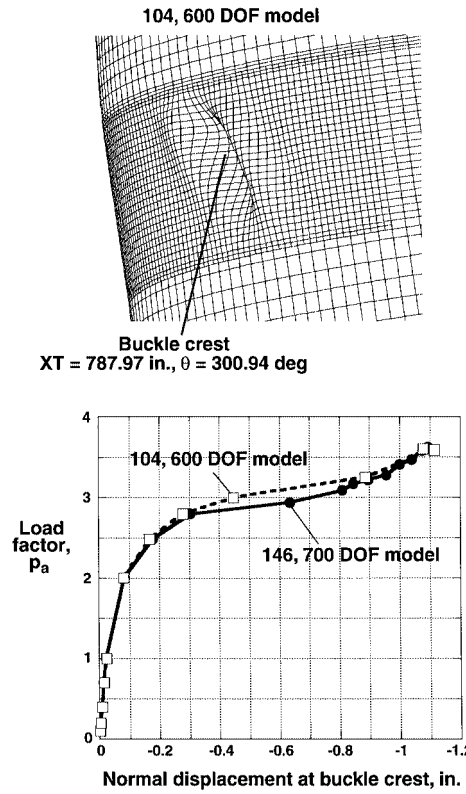

Fig. 7 Convergence of nonlinear solutions for prelaunch loading condition with full LH_2 and empty LO_2 tanks and imperfection-amplitude-to-shell-thickness ratio A/t = 0.25.

and solid lines shown in Fig. 7 correspond to the 104,600- and 146,700-DOF models, respectively. The unfilled square symbols and the filled circular symbols shown in Fig. 7 correspond to the discrete values of the load factor for the finite element results that were obtained with the 104,600- and 146,700-DOF models, respectively. The results shown in Fig. 7 indicate that there is a small discrepancy between the two nonlinear solutions. The solution for the more refined model has larger values of displacements for some values of the load factor, but the differences in the load factors for the two models is approximately 5% or less for all values of the normal displacement. This discrepancy is attributed to the fact that the less refined model overestimates the bending stiffness of the structure in the region of the buckle. The relatively small differences between the results in Fig. 7 suggest that the 146,700-DOF model is reasonably converged and adequate for conducting nonlinear analyses for this loading condition.

Results obtained from nonlinear analyses for a geometrically perfect shell and for geometrically imperfect shells with values for the imperfection-amplitude-to-wall-thickness ratio $A/t = 0.25, 0.5$, and 1.0 are shown in Fig. 8. These results were obtained with the 146,700-DOF model and with the imperfection shape in the form of the corresponding linear-bifurcation buckling mode with a negative amplitude. The filled circles indicate solutions for the geometrically perfect shell, and the unfilled squares, triangles, and circles indicate solutions for the geometrically imperfect shells with $A/t = 0.25$, 0.5, and 1.0, respectively. The horizontal dashed line represents the linear-bifurcation buckling load level. The results shown in Fig. 8 are presented as a plot of the load factor p_a vs the normal displacement of the shell wall at the largest crest of the buckle, defined by the coordinates $XT = 789.939$ in. and $\theta = 301.64$ deg.

The results in Fig. 8 indicate a significant reduction in the apparent meridional stiffness of the barrel section of the LO_2 tank, where the buckles appear, at a load factor slightly less than the linear-bifurcation buckling load level. These results also indicate that the barrel section of the LO_2 tank exhibits stable postbuckling load-carrying capacity for the geometrically imperfect shells and, as a result, is practically insensitive to initial imperfections.[10] Moreover, the shallowness of the barrel panel that contains the buckle and the

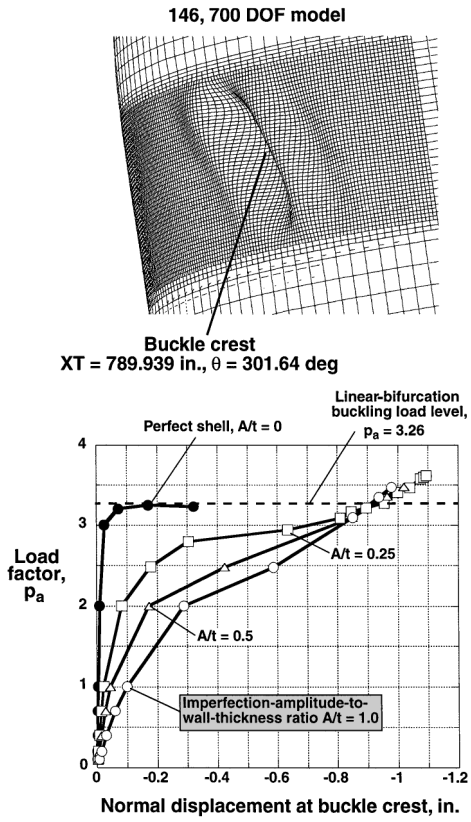

Fig. 8 Effect of imperfection amplitude on the nonlinear solutions for prelaunch loading condition with full LH_2 and empty LO_2 tanks.

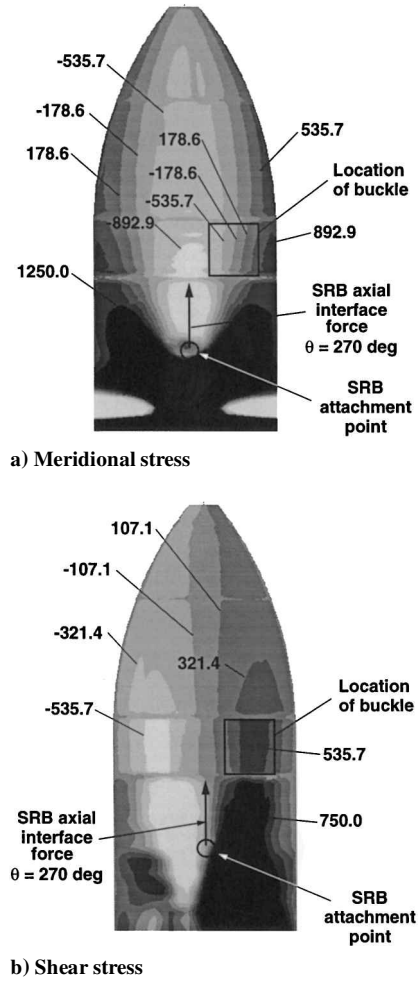

Fig. 9 Membrane stress distributions in geometrically perfect LO_2 tank and intertank for prelaunch loading condition with full LH_2 and empty LO_2 tanks; $p_a = p_b = 1$, stress values in pounds per square inch.

presence of stable postbuckling load-carrying capacity suggest that the buckling behavior is effectively like that of the stable-symmetric bifurcation type; that is, the unstable bifurcation behavior[10] usually associated with singly curved panels is essentially benign. For this type of nonlinear response, the linear-bifurcation buckling analysis gives a meaningful representation of the nonlinear response phenomena and gives a reasonable estimate of the buckling load level, especially for the smaller imperfection amplitudes. In this case, any use of a buckling-load knockdown factor would produce results that are overly conservative.

The buckle patterns obtained from the linear-bifurcation buckling analysis and the nonlinear analyses are all very similar in shape and occur in the same location. The stress distribution in the shell that causes the buckle pattern to form is shown in Fig. 9 for a geometrically perfect shell and for $p_a = p_b = 1$. Contours of the membrane meridional and shear stresses on the negative Y-axis side ($\theta = 270$ deg) of the tank are shown in Figs. 9a and 9b, respectively, in pound per square inch. These contours indicate that high meridional compression stresses exist in the thrust panel directly above the SRB attachment point, as expected. However, the thrust panels are massive and very stiff compared to the LO_2 tank shell and, as a result, do not buckle before the LO_2 tank. The contours also indicate that buckling occurs in a region of the barrel where there are significant shear stresses in the shell that interact with the meridional compressive stresses and reduce the buckling load.

Full LH_2 and LO_2 Tanks

The models investigated for this prelaunch loading condition ranged from 48,990 to 121,500 DOF. The model identified as adequate for predicting linear-bifurcation buckling that appears in Fig. 10 corresponds to 99,100 DOF. A 79,950-DOF model was investigated that has the same general mesh arrangement as that shown in Fig. 10, but the local refinement shown on the right side of the ogive was used for both locally refined regions of the ogive. The eigenvalues for the 79,950- and 99,100-DOF models are given by $p_a = 3.94$ and 3.78, respectively, where a value of 1.0 corresponds to the operational values of the destabilizing loads. Because of the smoothness of the buckling mode shown in Fig. 10 and the 4% difference in the eigenvalues, the 99,100-DOF model was used to represent the linear-bifurcation buckling behavior of the LO_2 tank for this loading condition. In addition, the ratio of the largest thickness in the area of the buckling mode shown in Fig. 10 to its smallest characteristic length is less than 0.1, which indicates that finite elements that are based on classical thin-shell theory are adequate. The 79,950- and 99,100-DOF models also were used to obtain nonlinear solutions for a geometrically perfect shell. The nonlinear solutions for these two models yield load vs normal displacement plots in which the difference in the load factors for the two models is approximately 4% or less for all values of the normal displacement. These solutions indicate that the 99,100-DOF model is reasonably converged and represents adequately the nonlinear behavior of the LO_2 tank for this loading condition. Thus, all subsequent results presented in this section were obtained with the 99,100-DOF model.

A short-wavelength buckle in the forward part of the aft ogive, shown in Fig. 10, is essentially a wrinkle in the skin on the negative Y-axis side of the tank. Here, the term short is used to indicate that the characteristic wavelength of the buckle pattern is small compared to the overall dimensions of the LO_2 tank. The loads acting along the shell meridians near the SRB attachment point develop the meridional compressive stress resultants shown in Fig. 11a (given in pounds per inch for $p_a = p_b = 1$) that caused the buckling mode shown in Fig. 10. Insight into the formation of the buckling mode is obtained by noting that Gaussian curvature is a geometric measure related to how much the shell membrane stiffness participates in its bending deformations. The results in Fig. 11 indicate that the meridional compressive stress resultants and the circumferential tension stress resultants increase in the LO_2 tank from the tip of the forward

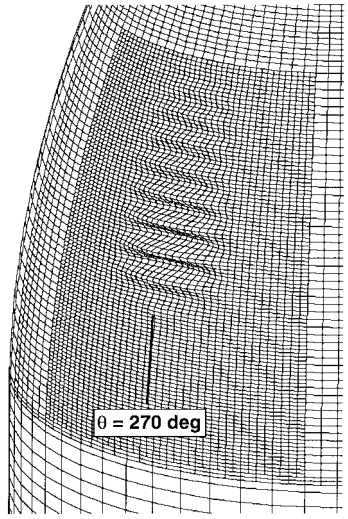

a) Rotated view

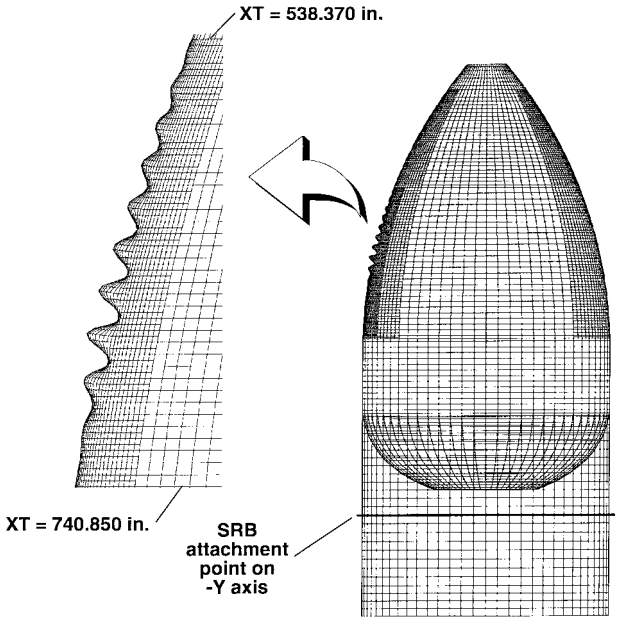

b) Side view

Fig. 10 Linear-bifurcation buckling mode for prelaunch loading condition with full LH_2 and LO_2 tanks; 99,100 DOF, $p_a = 3.78$, and $p_b = 1.0$.

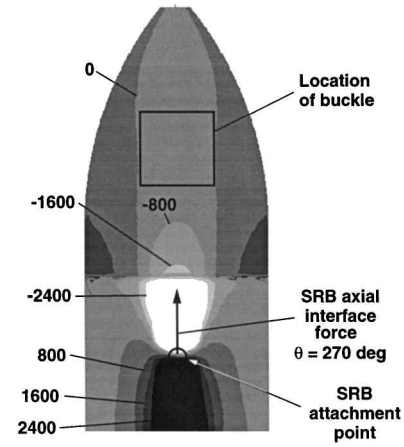

a) Meridional stress resultant

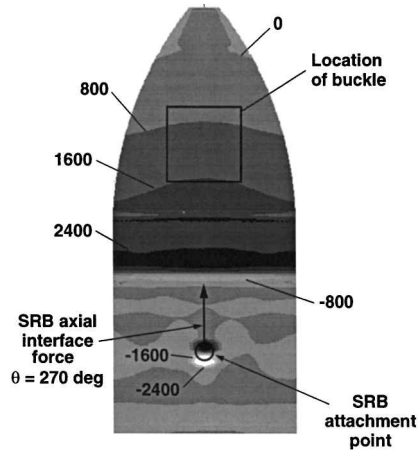

b) Circumferential stress resultant

Fig. 11 Stress distributions in geometrically perfect LO_2 tank and intertank for prelaunch loading condition with full LH_2 and LO_2 tanks; $p_a = p_b = 1$, stress resultant values in pounds per inch.

ogive to the intertank. The magnitude of the shell Gaussian curvature decreases in the aft ogive, which causes local buckling to occur at this location. In the forward ogive, there are relatively small values of hoop tensile stresses to stabilize the shell, but the Gaussian curvature is high. In the aft ogive, the meridional compressive stresses and hoop tensile stresses are larger than in the forward ogive, but the Gaussian curvature is much smaller. The STAGS results suggest that the higher values of meridional compressive stresses and lower values of Gaussian curvature in the aft ogive are the dominant factors that influence the location of the buckling mode. These findings also indicate that the shortness of the half-wavelength of the buckling mode is a result of the high values of the circumferential tensile stress resultants shown in Fig. 11 that are caused by the hydrostatic pressure exerted on the shell wall by the LO_2.

Results obtained from nonlinear analyses of a geometrically perfect shell and a geometrically imperfect shell with an imperfection-amplitude-to-wall-thickness ratio $A/t = 0.3$ are presented in Figs. 12 and 13, respectively. The thickness t in the ratio A/t is the minimum wall thickness of the aft ogive and has a value equal to 0.100 in. The results shown in Fig. 13 were obtained by using an imperfection shape that is in the form of the corresponding linear-bifurcation buckling mode with a negative amplitude. The results shown in Figs. 12 and 13 are for nonlinear solutions that were obtained by increasing the load factors p_a and p_b simultaneously to a value of one and then holding p_b constant while increasing the magnitude of the load factor p_a. The normal displacements along the length of the aft-ogive shell wall are represented by the solid lines in Figs. 12 and 13 for values of the load factor p_a approximately equal to 3.0, 4.0, and 5.0. Overall, negative values of the normal displacements are indicated by the left-hand-side ordinate for these three lines because of contraction of the aft ogive that is caused primarily by the LO_2 thermal load. The linear-bifurcation buckling mode is represented by the dashed line in Figs. 12 and 13 with normalized amplitudes given by the right-hand ordinate of the figures. The bifurcation mode in Figs. 12 and 13 shows the similarity between the nonlinear solution and the linear-bifurcation buckling mode and indicates how the imperfection shape influences the nonlinear solution. The solid lines shown in Figs. 12 and 13 predict a short-wavelength bending response in the aft ogive over the negative Y axis ($\theta = 270$ deg) that is similar in shape to the corresponding linear-bifurcation buckling mode shape, except at the ends of the aft ogive. The overall slope of the solid lines (obtained by fitting a straight line to each curve) in Figs. 12 and 13 is due to the outward displacement of the shell wall caused by the increase in pressure as p_a and p_b are simultaneously increased to a value of one in the nonlinear analysis. This nonlinear effect is inherently not represented in a linear-bifurcation buckling analysis and, as a result, the overall slope of the dashed lines is zero valued. Moreover, the bending deformations that appear at the ends of the aft ogive of the geometrically perfect shell are not captured by the linear-bifurcation buckling analysis. Thus, in a strict sense, the linear-bifurcation buckling analysis

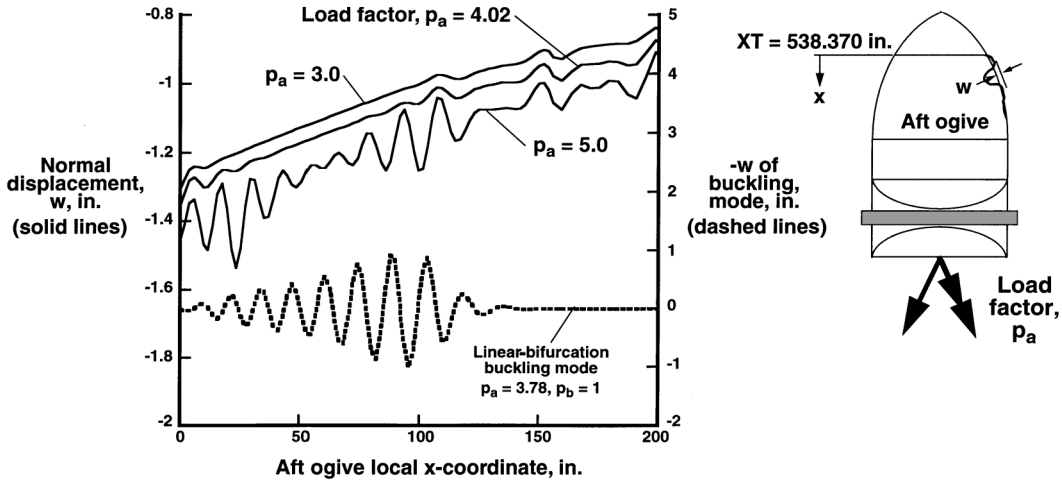

Fig. 12 Bending deformations in aft ogive of a geometrically perfect LO_2 tank shell for prelaunch loading condition with full LH_2 and LO_2 tanks; θ = 270 deg and p_b = 1.0.

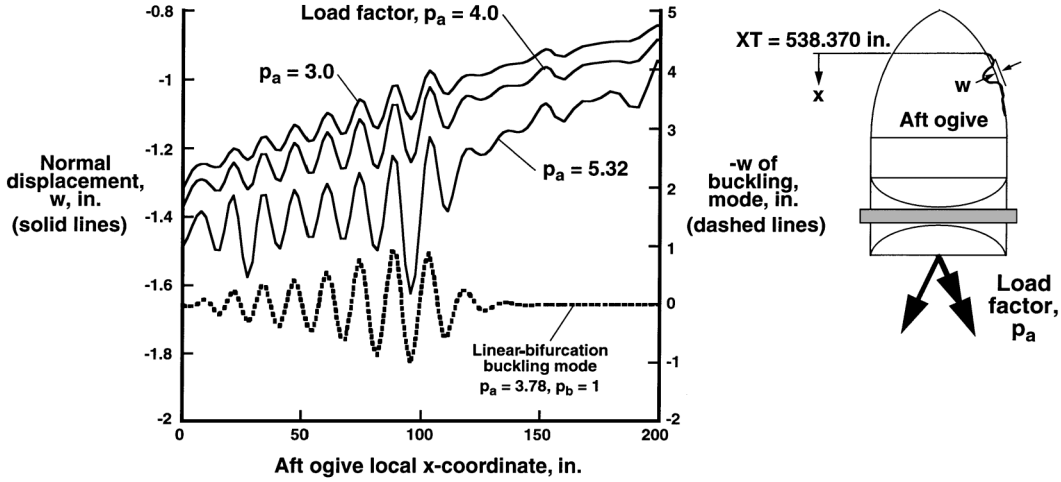

Fig. 13 Bending deformations in aft ogive of a geometrically imperfect LO_2 tank shell for prelaunch loading condition with full LH_2 and LO_2 tanks; θ = 270 deg, p_b = 1.0, and imperfection-amplitude-to-wall-thickness ratio A/t = 0.3.

does not represent accurately the nonlinear response phenomena for this loading condition.

The results presented in Figs. 12 and 13 predict a stable nonlinear response at load levels substantially greater than the load predicted by the linear-bifurcation buckling analysis ($p_a = 3.78$). This behavior shows that the use of a linear-bifurcation buckling analysis with a knockdown factor will yield overly conservative results for this loading condition. As the load increases, substantial bending deformations (indicated by the waviness of the curves) develop and grow in the shell wall, reducing the apparent meridional stiffness of the aft ogive. The nonuniformity of the bending deformations is caused by the thickness variations in the ogive and the presence of the weld lands. The results in Fig. 13 indicate that a geometrical imperfection in the shape of the linear-bifurcation buckling mode and with a small negative amplitude will greatly increase the severity of the bending deformations and will cause the growth of the bending deformations to start at much lower load levels. For the load levels considered, the von Mises stresses were well below the yield stress of the material.

The reduction in apparent meridional stiffness of the aft ogive is shown more explicitly in Fig. 14. In Fig. 14, the intensities of the bending deformations (indicated by the magnitude of the normal displacement amplitude) at $XT = 637.66$ in. for the geometrically perfect shell (see $x = 99.3$ in. in Fig. 12) and at $XT = 633.77$ in. for the geometrically imperfect shell (see $x = 95.4$ in. in Fig. 13) are given as a function of the load factor p_a. These locations represent the locations of the largest bending deformations shown in Figs. 12 and 13. The amplitude Δw shown in Fig. 14 is the distance from the maximum value of the local shell-wall displacement to the adjacent minimum value and represents the intensity of the local bending deformation in the response. The filled circles shown in Fig. 14 correspond to results for a geometrically perfect shell and the unfilled triangles and squares correspond to results for geometrically imperfect shells with imperfection-amplitude-to-wall-thickness ratios of $A/t = 0.1$ and 0.3, respectively ($t = 0.100$ in.). The horizontal dashed line shown in Fig. 14 represents the linear-bifurcation buckling load level.

The results shown in Fig. 14 indicate that the amplitude of the greatest local bending deformation grows with increasing load and that the amount of growth increases substantially with increasing geometric imperfection amplitude. The results predict that the shell can support loads greater than the critical buckling load predicted by a linear-bifurcation buckling analysis. As Δw increases, the apparent meridional stiffness decreases, and as a result, the positive-valued constant of proportionality between an increment in load and the corresponding increment in normal-displacement amplitude decreases. This trend is manifested by the reduction in slope of the load vs normal-displacement amplitude curves. This type of response is similar to the response reported by Stevens et al. in Ref. 11 for cylindrical shells subjected to combined internal pressure and a pure bending moment. The results in Ref. 11 indicate that the amplitude of the short-wavelength deflection approaches a horizontal tangent as the load increases and that the value of the load for the horizontal tangent corresponds to a local collapse mode of

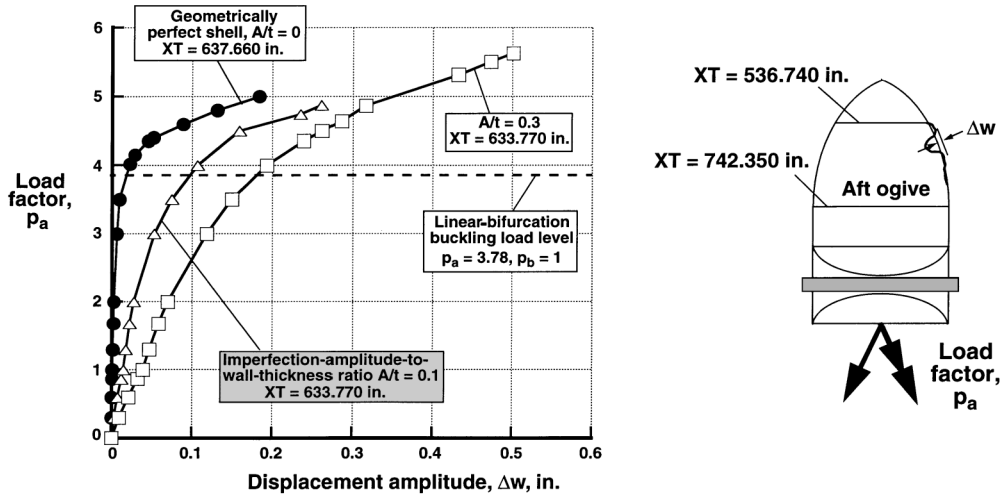

Fig. 14 Effect of imperfection amplitude on nonlinear solutions for prelaunch loading condition with full LH_2 and LO_2 tanks; θ = 270 deg and p_b = 1.0.

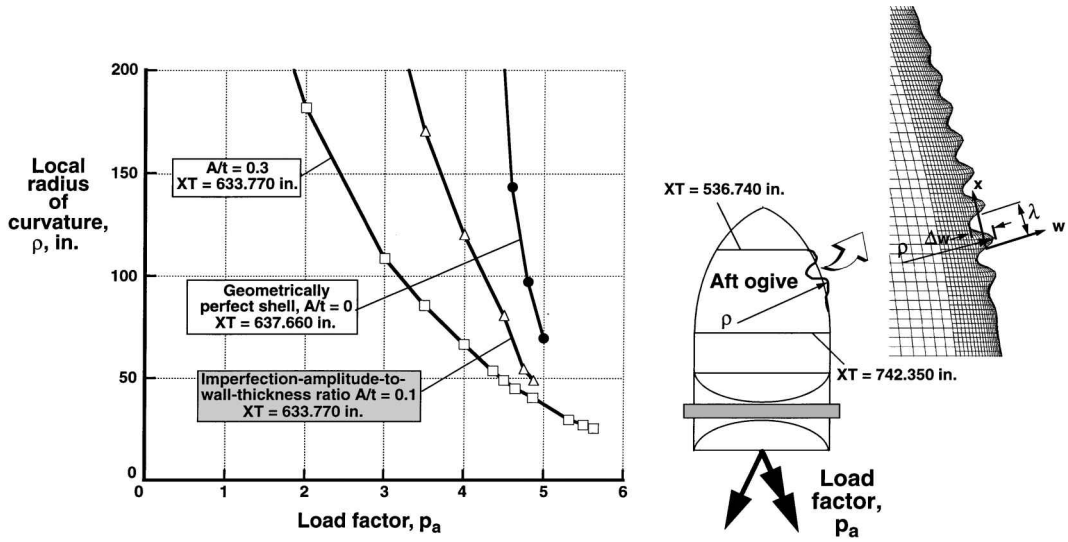

Fig. 15 Effect of imperfection amplitude on local radius of curvature of largest bending deformation for prelaunch loading condition with full LH_2 and LO_2 tanks; θ = 270 deg and p_b = 1.0.

the cylinder. Mathematically, the horizontal tangent indicates that unbounded growth of the displacement occurs for an infinitesimal increase in the load. The response displayed in Fig. 14 does not necessarily indicate approach of a horizontal tangent as Δw increases. In fact, the response for the geometrically perfect shell does not exhibit a significant change in apparent meridional stiffness at a load factor near the linear-bifurcation buckling load level, which again reinforces the statement that the linear-bifurcation buckling analysis does not represent accurately the nonlinear response. Unlike the response of a simple cylinder, substantial load redistribution may occur in this structure. If a horizontal tangent in a load vs displacement amplitude curve is approached, the region of the shell containing the bending deformations becomes incapable of supporting additional load, and the compressive load is redistributed to another portion of the aft ogive. If other parts of the ogive cannot support the redistributed compressive load, the shell will collapse. However, if other parts of the ogive can support the redistributed compressive load, the slope of the load vs displacement amplitude curve will increase as the loading increases. In general, geometric imperfections with large amplitudes also could cause a similar redistribution in load, and as a result, the corresponding slope of the load vs displacement amplitude curve would increase. This effect is a result of a reduction in the apparent membrane stiffness that occurs as the imperfection amplitude increases. Similar curves for smaller geometric imperfection amplitudes would approach a horizontal tangent.

In addition to results presented herein that were used to assess the stability of the SLWT LO_2 tank, the results presented in Figs. 12–14 were obtained to provide insight into the effect of the wrinklelike short-wavelength bending deformations on the behavior of the TPS. These results indicate that large local bending deformations may occur in the shell wall for loads that are much smaller than the local collapse load and may cause the TPS to debond from the shell wall and fail. The results presented in Fig. 15 indicate approximate estimates of the local radius of curvature for the largest bending deformation in the aft ogive along the negative Y axis ($\theta = 270$ deg). These bending deformations are located at $XT = 637.66$ in. for the geometrically perfect shell (see $x = 99.3$ in. in Fig. 12) and at $XT = 633.77$ in. for the geometrically imperfect shells (see $x = 95.4$ in. in Fig. 13). The local radius of curvature ρ shown in the right-hand sketch of Fig. 15 is calculated by the formula

$$\rho = [1 + (w')^2]^{\frac{3}{2}} / |w''| \tag{9}$$

where w, the local displacement shown in the right-hand side in Fig. 15, is approximated by

$$w = (\Delta w/2)\sin(2\pi x/\lambda) \tag{10}$$

where λ is the buckle wavelength and Δw is the deformation amplitude (see Fig. 14). The prime marks denote differentiation with respect to the local x coordinate. At the crests of the wave defined

by $x = \lambda/4$ and $3\lambda/4$, $w' = 0$, and the radius of curvature is given by

$$\rho = \lambda^2/(2\pi^2 \Delta w) \tag{11}$$

The values of ρ were calculated, for each value of XT that corresponds to the largest bending deformation in the aft ogive, by determining λ and Δw from the corresponding finite element results and then substituting these values into Eq. (11). The filled circles shown in Fig. 15 correspond to results for the geometrically perfect shell, and the unfilled triangles and squares correspond to results for geometrically imperfect shells with imperfection-amplitude-to-wall-thickness ratios of $A/t = 0.1$ and 0.3, respectively. The imperfection shape is identical to the linear-bifurcation buckling mode with a negative amplitude shown in Fig. 10. The results in Fig. 15 demonstrate that the geometric imperfection amplitude has a significant influence on the local radius of curvature of the deformed shell wall. For example, if a given thermal protection system is known to debond from the shell wall at a value of $\rho = 100$ in., the maximum load factor is reduced from a value of approximately 4.8 for the geometrically perfect shell to 3.2 for the geometrically imperfect shell with $A/t = 0.3$.

SWT Tank Full-Scale Structural Test Results

To obtain confidence in the STAGS modeling approach used for the SLWT LO_2 tank, finite element analyses were performed for two full-scale structural tests with the same modeling approach that was used for the SLWT LO_2 tank. These two tests are the only experimental data available for any Space Shuttle LO_2 tank that exhibited a buckling event. The two full-scale tests were conducted approximately 20 years ago at the NASA Marshall Space Flight Center on the original SWT LO_2 tank during the development program of the original Space Shuttle ET, and both test articles buckled unexpectedly. Because buckling was unexpected, measurements of initial geometric imperfections in the tank wall were not made for either of these test specimens. As a result, these test results cannot be used quantitatively as an absolute measure of the accuracy of the STAGS models of the SLWT LO_2 tank. However, adequacy of, and confidence in, the STAGS models are obtained if the location of the buckle pattern observed in each test is predicted accurately and the corresponding buckling load is bounded by the finite element analysis predictions for a geometrically perfect shell and a shell with a severe initial geometric imperfection in the form of the linear-bifurcation mode that has an amplitude of one nominal, minimum-gauge wall thickness. Although these two conditions do not represent strictly sufficient conditions for the absolute accuracy of the finite element models, it was rationalized by the SLWT tank structural verification team that they do represent necessary conditions for the finite element analyses and should be met. In particular, if the finite element models are in error to the extent that they represent inadequately the membrane and bending stiffnesses of the structure and the internal load distribution, it is most likely that these two conditions could not be met.

The SWT LO_2 tank has essentially the same geometry as the SLWT LO_2 tank, but is made of 2219 aluminum alloy. The primary difference between the two LO_2 tanks is that the skins of the SWT tank are thicker than those of the SLWT tank, with the thicknesses much more uniformly distributed over the SWT tank shell. Thus, the modeling approach described earlier for the SLWT tank was used to model the two full-scale SWT tank test articles, and the behavior of the SWT tank has a direct relationship with the behavior of the SLWT tank. The SWT tank model was generated by modifying the STAGS userwritten subroutine[3] that was used to describe the thickness distribution of the SLWT tank to account for the SWT tank thicknesses and by changing the material properties. The SLWT tank structural verification team indicated that the differences between the SWT intertank and the SLWT intertank are negligible with respect to the transfer of loads from the intertank to the LO_2 tank. As a result of this information, the SLWT intertank part of the finite element models was not modified. The two full-scale SWT tank tests described subsequently are referred to herein as the structural test article (STA) and the ground vibration test article (GVTA).

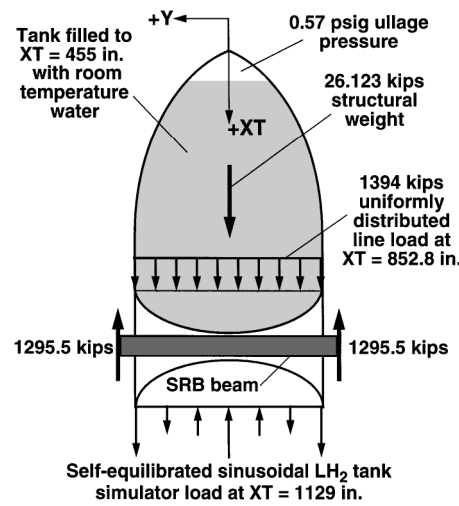

Fig. 16 Loads for SWT tank STA at buckling.

STA Results

The STA consisted of a SWT LO_2 tank and a SWT intertank mounted vertically to a LH_2 tank load simulator and two rigid vertical posts at the SRB attachment points. The LH_2 tank load simulator was modeled by a self-equilibrated line load that is applied to the bottom of the intertank and varies sinusoidally around the circumference, as depicted in Fig. 16. A uniformly distributed circumferential line load of 1394 kips was also applied to the tank at $XT = 852.8$ in. During the test, these two loads were applied first and then the tank was filled with room temperature water while an ullage pressure was maintained in the tank. After filling the tank to $XT = 455$ in., a depth of approximately 42 ft, the ullage pressure was slowly reduced. When the ullage pressure reached 0.57 psi gauge pressure, the tank unexpectedly buckled in the forward ogive between $XT = 455$ and 475 in. and between $\theta = 253$ and 277 deg (negative Y-axis side of the tank). The SRB interface forces that are reacted at the two vertical posts had magnitudes equal to 1295 kips (Fig. 16).

To simulate the test loading conditions in a practical manner, all loads shown in Fig. 16, except for the SRB beam loads, were controlled in the analysis by a load factor p_a. A value of $p_a = 1$ corresponds to values of the loads at which the actual test article buckled. Finite element models were constructed for the STA in which the tank was supported at the ends of the SRB beam and the loads at the ends of the SRB beam were computed as reactions. These reactions were found to be in excellent agreement (differences of less than 1%) with the corresponding specified SRB beam loads shown in Fig. 16, which indicates that finite element modeling details, such as the mass distribution and applied loads, are represented accurately.

A limited convergence study was also performed with several finite element models of the STA. The final model that was used to analyze the STA has 159,993 DOF and is highly refined in the forward ogive on the negative Y-axis side of the tank. The linear-bifurcation buckling mode obtained for the STA with this mesh is shown in Fig. 17 and is a short-wavelength buckle, with respect to the size of the forward ogive. Once again, the ratio of the largest thickness in the area of the buckling mode to its smallest characteristic length is less than 0.1, which indicates that finite elements that are based on classical thin-shell theory are adequate. The location of the linear-bifurcation buckling mode shown in Fig. 17 is the same as the location observed during the test. The eigenvalue for this linear-bifurcation mode is given by $p_a = 1.14$.

Next, a series of nonlinear analyses were conducted with the 159,993-DOF model for values of the imperfection-amplitude-to-wall-thickness ratio $A/t = 0$, 0.1, 0.25, 0.5, and 1.0. The thickness t in the ratio A/t is the minimum wall thickness of the forward ogive and has a value equal to 0.080 in. For each of these cases, the geometric imperfection shape was input in the form of the linear-bifurcation buckling mode shown in Fig. 17, with a negative amplitude.

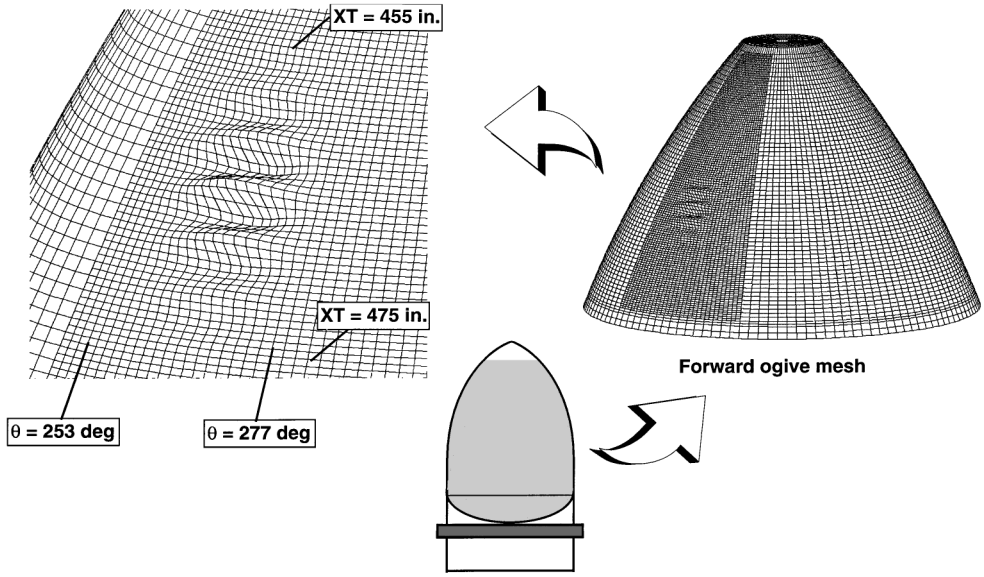

Fig. 17 Linear-bifurcation buckling mode for the STA; 159,993 DOF and p_a = 1.14.

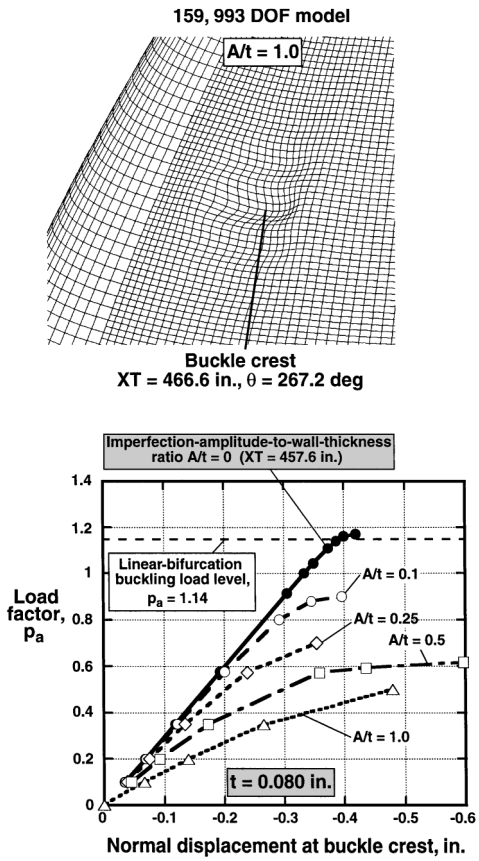

Fig. 18 Effect of imperfection amplitude on the buckling load for the STA.

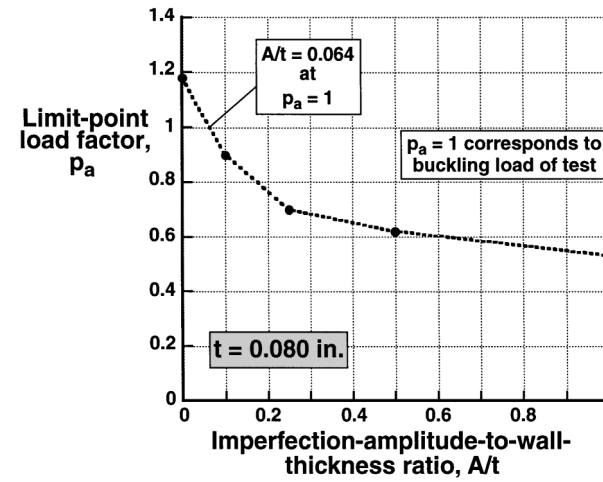

Fig. 19 Predicted imperfection sensitivity of the STA.

Figure 18 shows the results of the nonlinear analyses of the STA. The maximum normal displacement that occurs at the crest of the buckle pattern is shown in Fig. 18 as a function of the load factor p_a. The buckle crest is located at $XT = 457.6$ and 466.6 in. for the geometrically perfect and imperfect shells, respectively, and at $\theta = 267.2$ deg. The filled circles and the unfilled circles, diamonds, squares, and triangles correspond to results for $A/t = 0$, 0.1, 0.25, 0.5, and 1.0, respectively. The horizontal dashed line represents the linear-bifurcation buckling load level. The results for all values of A/t indicate a monotonic increase in normal displacement with increasing load. For each case, the load factor vs normal-displacement curve approaches a horizontal tangent as the load factor increases, which indicates an incipient limit-point or snap-through response of the shell. The characterization of the shell response as a limit-point or snap-through response is also justified by the fact that the value of the limit-point load factor decreases with increasing imperfection amplitude. At each limit point, the shell exhibited relatively large inward normal displacements and substantial bending deformations (particularly for $A/t = 1.0$) at the same location of the linear-bifurcation buckling mode shown in Fig. 17, which is compatible with an incipient snap-through buckling response at this location. The actual nonlinear deformation pattern for the limit point (prior to snap through) that was obtained from a nonlinear analysis of the STA with $A/t = 1.0$ is shown in Fig. 18, and the ratio of the deformation pattern's largest thickness to its smallest characteristic length is less than 0.1. The meridional and circumferential stress resultant distributions are similar to those presented in Fig. 11 for the prelaunch loading condition with full LH_2 and LO_2 tanks.

The values of the limit points are shown in Fig. 19 as a function of geometric imperfection amplitude and load factor, and indicate the imperfection sensitivity of the forward ogive of the STA. The limit points that were obtained for the STA span a broad load range bounded by $p_a = 1.18$ for a geometrically perfect shell and $p_a = 0.53$ for a geometrically imperfect shell with $A/t = 1.0$ ($A = 0.080$ in.) and a severe, linear-bifurcation-mode imperfection shape. This load range corresponds to a 55% reduction in load-carrying capacity of a geometrically perfect shell. The similarity

between the linear-bifurcation buckling mode and the deformation pattern obtained from the nonlinear analysis of the geometrically perfect shell, the coincidence of their locations, and the approximately 3.5% difference between the linear-bifurcation-buckling eigenvalue and the limit-load level for the geometrically perfect shell, indicate that the linear-bifurcation analysis characterizes adequately the nonlinear response phenomena exhibited by the STA. In addition, the small difference between the linear-bifurcation-buckling eigenvalue and the limit-load level for the geometrically perfect shell indicates a small stiffening effect that is caused by geometrically nonlinear prebuckling deformations. The 55% reduction in load-carrying capacity of a geometrically perfect shell that is caused by the inital geometric imperfections considered corresponds to a linear-bifurcation buckling-load knockdown factor approximately equal to 0.46.

The dashed line shown in Fig. 19 has a value of $A/t = 0.064$ for $p_a = 1$ (which corresponds to the buckling load of the test), which is bounded by the analytical results for $A/t = 0$ and 1. This result, and the accurate prediction of the buckle location, suggest that the STAGS modeling approach described herein provides a reasonably accurate indication of the SWT LO_2 tank behavior. More specifically, the results suggest that the modeling approach captures the membrane and bending stiffnesses and the internal load path adequately, and should be applicable to similar loading conditions. In particular, the buckling-load level that is obtained for the geometrically perfect structure must be greater than that observed for the tests because of the inherent presence of small initial geometric imperfections that generally tend to reduce the buckling load of thin-walled shells. In addition, an imperfection amplitude of one minimum-gauge wall thickness is considered to be at the border of amplitudes that are considered to be small. Thus, if a large amplitude is needed to bound the test results, it is likely that the finite element model has a significant deficiency. Because of the high degree of similarity between the SWT and SLWT LO_2 tanks, the results suggest that the SLWT tank models should capture adequately the actual LO_2 tank membrane and bending stiffnesses and, as a result, provide a reasonable representation of the SLWT LO_2 tank nonlinear shell response.

GVTA Results

The GVTA consisted of a SWT tank mounted on two SRBs and an orbiter attached to the SWT tank. The SWT tank consisted of a LO_2 tank, a LH_2 tank, and an intertank. In this configuration, the SWT tank is inclined at an angle of approximately 10 deg in the XT–Z plane because of the eccentric weight of the orbiter. The loads that act on the LO_2 tank and intertank during the test and the inclination angle $\alpha = 10$ deg are shown in Fig. 20. These loads were supplied by the SLWT tank structural verification team and consist of two SRB interface force components, the LH_2 tank interface force and moment, a uniformly distributed circumferential line load of 20.86 kips applied at $XT = 852.8$ in., and a hydrostatic water pressure distribution that corresponds to the tank fill level of $XT = 645$ in. (a depth of approximately 26.5 ft). No ullage pressure was present inside the LO_2 tank during the test. The hydrostatic pressure distribution for the GVTA was defined in the STAGS models with a user-written subroutine in terms of the local axial coordinate x shown in Fig. 20b. The pressure distribution is given by $p(x, \theta) = 0$ for values of $x \leq x_f - r(x) \tan\alpha \cos\theta$, where x_f is the local coordinate of the fill level that is defined by the positive numerical difference between stations $XT = 645$ and 371 in., as shown in Fig. 20b. The symbol θ is the cylindrical coordinate defined in Fig. 2, and $r(x)$ is the polar radius of the shell reference surface (see Fig. 20b) that was calculated from the differential geometry of the LO_2 tank components. For the remaining values of x, the pressure is given by

$$p(x, \theta) = \gamma[(x - x_f)\cos\alpha + r(x)\sin\alpha\cos\theta] \qquad (12)$$

where γ is the specific weight of water at room temperature.

The original test plan for the GVTA was to fill the tank with water and then to perform a ground vibration test. However, when the water level reached $XT = 645$ in., the tank buckled unexpectedly in the forward ogive between approximately $XT = 437$ and 503 in. and between $\theta = 247$ and 281 deg (negative Y-axis side of the tank).

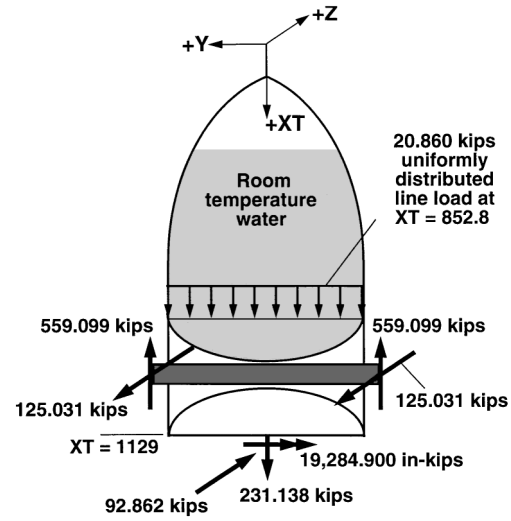

a) Front view

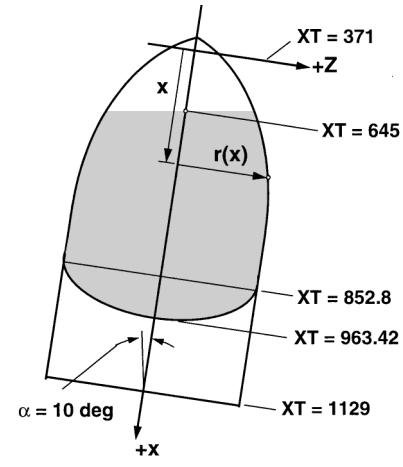

b) Side view

Fig. 20 Loads for SWT tank GVTA at buckling; *XT* values in inches.

The test loading conditions for the GVTA were simulated in the manner described herein for the STA; that is, all loads shown in Fig. 20, except for the SRB interface forces, were assigned to a load factor p_a such that a value of $p_a = 1$ corresponds to buckling of the test article. Several finite element models were constructed for the GVTA in which the tank was supported at the ends of the SRB beam and the loads at the ends of the SRB beam were computed as reactions. These reactions were found to be in very good agreement (to within approximately 4%) with the specified SRB interface forces shown in Fig. 20a.

A limitied convergence study was performed with several finite element models of the GVTA. The final model selected to analyze the GVTA has 252,300 DOF and is highly refined in the forward ogive on the negative Y-axis side of the tank. The linear-bifurcation buckling mode obtained for the GVTA with this mesh is shown in Fig. 21. This buckling mode is also a short-wavelength buckling mode similar to the one obtained for the STA. The location of the linear-bifurcation buckling mode shown in Fig. 21 is essentially the same as the location of the buckle that was observed during the test. The eigenvalue is given by $p_a = 2.41$.

Next, the 252,300-DOF model was used to conduct nonlinear analyses for values of the imperfection-amplitude-to-wall-thickness ratio $A/t = 0$, 0.125, 0.25, 0.5, 0.75, and 1.0. The minimum wall thickness t for the forward ogive has a value equal to 0.080 in. For each of these cases, the geometric imperfection shape was in the form of the linear-bifurcation buckling mode shown in Fig. 21, with a negative amplitude.

The results of the nonlinear analyses of the GVTA are shown in Fig. 22. The maximum normal displacement that occurs at the

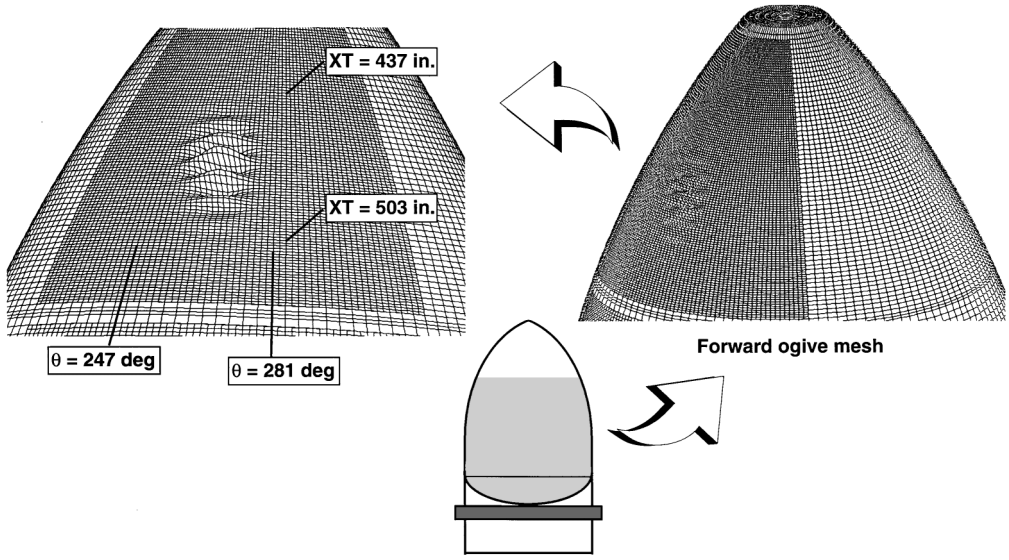

Fig. 21 Linear-bifurcation buckling mode for the GVTA; 252,300 DOF and p_a = 2.41.

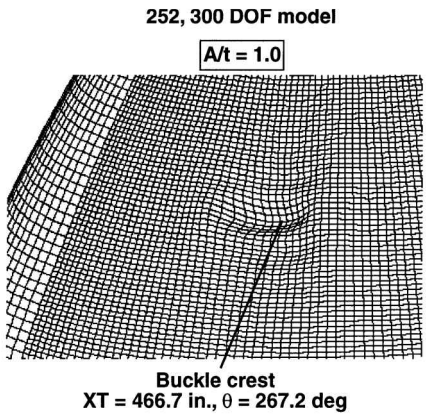

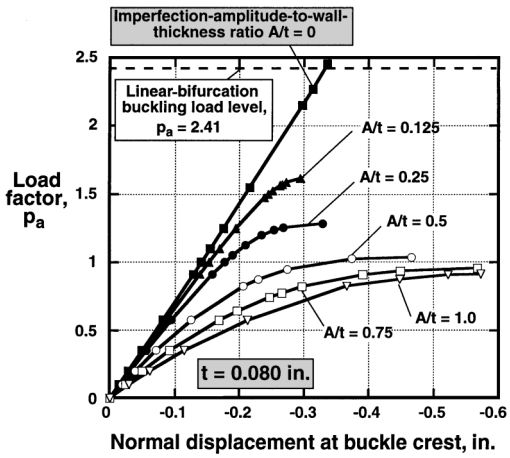

Fig. 22 Effect of imperfection amplitude on the buckling load for the GVTA.

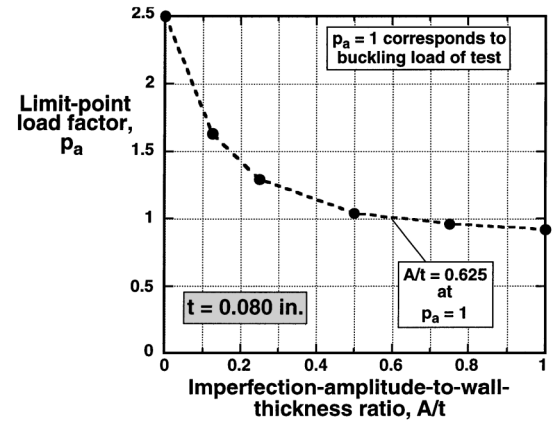

Fig. 23 Predicted imperfection sensitivity of the GVTA.

crest of the buckle pattern is located at $XT = 466.7$ in. and at $\theta = 267.2$ deg and is shown in Fig. 22 as a function of the load factor p_a. The filled squares, triangles, and circles and the unfilled circles, squares, and triangles correspond to results for $A/t = 0, 0.125, 0.25, 0.5, 0.75$, and 1.0, respectively. The horizontal dashed line represents the linear-bifurcation buckling load level. Similar to the STA results, the GVTA results indicate a monotonic increase in load with increasing normal displacement that terminates at a limit point for all nonzero values of A/t. At each limit point, the shell exhibited relatively large inward normal displacements and substantial bending deformations (particularly for $A/t = 1.0$) at the same location of the linear-bifurcation buckling mode shown in Fig. 21, which is consistent with an incipient snap-through buckling response at this location. The actual nonlinear deformation pattern that corresponds to the limit point that was obtained from a nonlinear analysis of the GVTA with $A/t = 1.0$ is shown in Fig. 22. The ratio of the deformation pattern's largest thickness to its smallest characteristic length is less than 0.1, which indicates that finite elements that are based on classical thin-shell theory are adequate. The values of the limit points displayed in Fig. 22 are shown in Fig. 23 (filled circles) as a function of the geometric imperfection amplitude and load factor to indicate the imperfection sensitivity of the GVTA. The limit points obtained for the GVTA span a broad load range bounded by $p_a = 2.46$ for a geometrically perfect shell and $p_a = 0.92$ for a geometrically imperfect shell with $A/t = 1$. This load range corresponds to a 62% reduction in load-carrying capacity of a geometrically perfect shell. The load reduction predicted for the GVTA is approximately 7% greater than that for the STA, and is attributed to the difference in the loading conditions. The approximately 2% difference in the limit load for the geometrically perfect shell and the linear-bifurcation eigenvalue is again attributed to a small effect of geometric nonlinearity. As for the STA, the similarity between the linear-bifurcation buckling mode and the deformation pattern obtained from the nonlinear analysis of the geometrically perfect shell, the coincidence of their locations, and the approximately 2% difference between the linear-bifurcation-buckling eigenvalue and the limit-load level for the geometrically perfect shell, indicate that the linear-bifurcation analyses characterizes adequately the nonlinear response phenomena exhibited by the GVTA. The 62% reduction in

load-carrying capacity of a geometrically perfect shell that is caused by the inital geometric imperfections considered corresponds to a linear-bifurcation buckling load knockdown factor approximately equal to 0.38.

The dashed line shown in Fig. 23 has a value of $A/t = 0.625$ ($A = 0.0504$ in.) for $p_a = 1$ (which corresponds to the buckling load of the test). Because of the accurate prediction of the buckle location and the prediction of reasonable bounds on the experimental buckling-load level, the results for the GVTA also suggest that the STAGS modeling approach captures the stiffness and internal load paths well enough to provide reasonably accurate indications of the SWT, and hence the SLWT, LO_2 tank nonlinear shell responses.

Concluding Remarks

Buckling and nonlinear analyses of the Space Shuttle SLWT LO_2 tank have been presented. An overview of the LO_2 tank and intertank structures has been presented, the loading details for two important prelaunch loading conditions have been described, and the method used in the present study to simulate these loading conditions has been discussed. In addition, the analysis code that has been used at the NASA Langley Research Center for linear-bifurcation buckling and nonlinear analyses of the SLWT LO_2 tank has been briefly described.

Results have been presented herein for the SLWT LO_2 tank that is subjected to two prelaunch loading conditions and for two full-scale structural tests that were conducted during the development program of the original SWT tank approximately 20 years ago. The SWT LO_2 tank has essentially the same geometry as the 2195 aluminum–lithium SLWT LO_2 tank, but is made of 2219 aluminum alloy. The primary difference between the two LO_2 tanks is that the skins of the SWT tank are thicker than those of the SLWT tank, with the thicknesses much more uniformly distributed over the SWT tank shell. These results have illustrated three distinctly different types of nonlinear response phenomena for thin-walled shells subjected to combined mechanical and thermal loads that may be encountered in the design of other liquid-fuel launch vehicles and that should be considered in the design of a TPS. In addition, a discussion of the applicability of linear-bifurcation buckling analyses to the characterization of the three nonlinear response phenomena has been given. Moreover, the results have indicated that meaningful predictions of the response of these shells generally require large-scale, high-fidelity finite element models. This need results from the presence of localized, short-wavelength response phenomena in a relatively large structure that are caused primarily by circumferential tension stresses that are associated with internal ullage and fuel pressures. Use of coarse finite element models for similar problems could miss a similar response mode entirely.

For the first SLWT tank prelaunch loading condition, the LH_2 tank is full and the LO_2 tank is empty. The finite element results predict that the nonlinear response is characterized by a platelike or very shallow curved-panel-like buckling response that is essentially insensitive to initial geometric imperfections. The results also indicate that for this type of launch-vehicle response phenomenon, linear-bifurcation analyses yield a reasonable characterization of the nonlinear response. For this loading condition, the barrel section of the LO_2 tank is predicted to buckle at loads that are more than twice the operational destabilizing loads.

For the second SLWT tank prelaunch loading condition, the LH_2 and LO_2 tanks are full. The nonlinear response for this loading condition is characterized by a short-wavelength bending deformation that grows in amplitude in a stable manner with increasing load. For this loading condition, local bending deformations appear in the aft ogive of the LO_2 tank that do not lead to a general instability mode but may cause failure of the TPS for load levels in excess of approximately twice the operational load level. Results have been presented in the present paper that can be used to estimate the load level at which the TPS may become damaged. Moreover, the results predict that the severity of the local deformations is significantly affected by localized initial geometric imperfections. For this type of launch-vehicle response phenomenon, the linear-bifurcation buckling analyses do not represent adequately the mechanics of the actual shell response, and underestimate signficantly the elastic load-carrying capacity of the structure. In particular, the linear-bifurcation buckling analyses did not predict some significant local bending deformations that develop near the ends of the aft ogive and that could affect significantly the performance of the TPS. For problems of this type, the use of shell stability knockdown factors with linear-bifurcation buckling results would be overly conservative.

For the two full-scale structural tests of the SWT, the nonlinear responses exhibit local buckling of a doubly curved shell segment of the LO_2 tank forward ogive that is characterized by a limit-point or snap-through behavior. The accurate prediction of the buckle pattern locations that were obtained from the linear-bifurcation analysis and from the nonlinear analysis of the geometrically perfect GVTA shell, and the small difference between the linear-bifurcation-buckling eigenvalue and the limit-load level for the geometrically perfect shell, indicate that the linear-bifurcation analyses adequately characterize the nonlinear response phenomena exhibited by the two tests. The magnitude of the load level that corresponds to the limit point has been shown to be very sensitive to local initial geometric imperfections in the LO_2 tank. Specifically, load reductions of about 55–62% of the buckling load of a geometrically perfect shell are predicted for a geometric imperfection shape in the form of the linear-bifurcation-buckling mode and with a one-wall-thickness imperfection amplitude. The 55 and 62% reduction in load-carrying capacity corresponds to linear-bifurcation buckling-load knockdown factors approximately equal to 0.46 and 0.38, respectively.

The buckling loads that were obtained from the highly refined finite element models for both tests correspond to geometric imperfection amplitudes that are greater than zero and less than one minimum-gauge wall thickness. This result implies that the finite element models capture adequately the membrane and bending stiffnesses and the internal load path of the SWT LO_2 tank. In particular, the buckling-load level that is obtained for the geometrically perfect structure must be greater than that observed for the tests because of the inherent presence of small initial geometric imperfections and the fact that, in many cases, small initial geometric imperfections are known to cause substantial reductions in the buckling resistance of thin-walled shells. In addition, an imperfection amplitude of one minimum-gauge wall thickness is considered to be at the border of amplitudes that are considered to be small. Thus, if a large amplitude is needed to bound the test results, it is likely that the finite element model has a significant deficiency. Moreover, the location of the buckles was predicted to be in essentially the same location that was observed for each test. Thus, the finite element results for the two full-scale tests, and the high degree of similarity between the SWT and SLWT LO_2 tanks, suggest that the finite element modeling approach used in the present study should represent the nonlinear behavior of the SLWT LO_2 tank reasonably well.

Acknowledgments

The authors would like to express their thanks to Walter L. Heard Jr. (retired), Charles C. Rankin, Michael Quiggle and Gale Copeland, and Neil Otte and Robert S. Ryan (retired) of NASA Langley Research Center, Lockheed Martin Missiles and Space Company, Lockheed Martin Manned Space Systems Division, and the NASA Marshall Space Flight Center, respectively, for their technical support.

References

[1] Spier, E. E., and Heller, G. D., "General Collapse and Joint Analysis of a Launch Vehicle Graphite/Epoxy Conical Adapter," *3rd NASA/USAF Conference on Fibrous Composites in Flight Vehicle Design*, Pt. 1, NASA TM X-3377, 1976, pp. 305–333.

[2] Young, R. D., and Rankin, C. C., "Modeling and Nonlinear Structural Analysis of a Large-Scale Launch Vehicle," *Journal of Spacecraft and Rockets*, Vol. 36, No. 6, 1999, pp. 804–811.

[3] Brogan, F. A., Rankin, C. C., and Cabiness, H. D., *STAGS User Manual*, Lockheed Martin Missiles and Space Co., Rept. LMSC P032594, Palo Alto, CA, June 1994.

[4] Simmonds, J. G., "An Improved Estimate for the Error in the Classical, Linear Theory of Plate Bending," *Quarterly of Applied Mathematics*, Vol. 29, No. 3, 1971, pp. 439-447.

[5]Stein, M., and Bains, N. J. C., "Postbuckling Behavior of Longitudinally Compressed Orthotropic Plates with Three-Dimensional Flexibility," AIAA Paper 86-0976, May 1986.

[6]Stein, M., "Effects of Transverse Shearing Flexibility on Postbuckling of Plates in Shear," *AIAA Journal*, Vol. 27, No. 5, 1989, pp. 652–655.

[7]Nemeth, M. P., Britt, V. O., Collins, T. J., and Starnes, J. H., Jr., "Nonlinear Analysis of the Space Shuttle Superlightweight External Fuel Tank," NASA TP 3616, Dec. 1996.

[8]Bushnell, D., "Computerized Analysis of Shells—Governing Equations," *Computers and Structures*, Vol. 18, No. 3, 1984, pp. 471–536.

[9]Seide, P., "A Reexamination of Koiter's Theory of Initial Postbuckling Behavior and Imperfection Sensitivity of Structures," *Thin-Shell Structures: Theory, Experiment, and Design*, edited by Y. C. Fung and E. E. Sechler, Prentice–Hall, Upper Saddle River, NJ, 1974, p. 69.

[10]Bushnell, D., *Computerized Buckling Analysis of Shells*, Kluwer Academic, Norwell, MA, 1989, pp. 1–29.

[11]Stephens, W. B., Starnes, J. H., Jr., and Almroth, B. O., "Collapse of Long Cylindrical Shells Under Combined Bending and Pressure Loads," *AIAA Journal*, Vol. 13, No. 1, 1975, pp. 20–25.

H. L. McManus
Associate Editor